



Spatiotemporal Ground Risk Mapping for Uncrewed Aerial Systems Operations

Aliaksei Pilko*, András Sóbester†, James P. Scanlan‡ and Mario Ferraro§
University of Southampton, Southampton, SO17 1BJ, United Kingdom

In this paper we propose the use of spatiotemporal population density data in the analysis of ground risk posed by UAS (Uncrewed Aerial System) operations. The spatiotemporal population density maps are generated through the combination of authoritative data sources, open source geospatial databases, and past works to dynamically classify proportions of a population to their expected daily activities based upon a given time. This adds a further dimension to analysis allowing evaluation and optimisation of ground risk, both spatially and temporally. This approach is used to analyse the ground risk posed under ballistic and gliding descents of a parameterized UAS along a case study path. An open source tool is implemented as part of this work to aid the decision making of operators and promote safer UAS operations.

I. Introduction

Uncrewed Aerial System (UAS) use is increasing rapidly in terms of operational numbers and mission diversity, resulting in increasing regulatory workload for UAS operators and aviation authorities. A core component of this is the Specific Operational Risk Assessment (SORA), which must include an objective assessment of the risk the UAS poses to, amongst others, third parties that may be overflown or are in the vicinity of the flight path and may reasonably be affected by UAS operations.

The United Kingdom Civil Aviation Authority (CAA) sets out broadly similar regulations as the European Union with regard to the classification of UAS [1]. The Single European Sky ATM Research Concept of Operations for European UTM Systems (SESAR CORUS) project [2] builds on the previous SESAR Uncrewed Traffic Management (UTM) projects such as the Air Traffic Management (ATM) Master Plan [3] and U-Space blueprint to create a unified Concept of Operations. This includes a categorisation of UAS and their operations broadly by level of risk involved with operations within that particular category. The European Aviation Safety Agency (EASA) has specified three broad categories for UAS operations which are mirrored by CAA regulations [2, 4]. In order of ascending perceived risk level they are Open, Specific and Certified. The Open category has further subdivisions, as this category may broadly be considered conventional consumer UAS. The subsequent categories are subject to specific scrutiny of the operations and require accompanying documentation such as the SORA, including the third party ground risk assessment, in order to be allowed to operate.

Current operational ground risk assessment can be subjective and assesses the risk posed based on qualitative categories of risk with notional probability ranges, therefore are prone to human error, as well as requiring large quantities of supporting documentation to be submitted for review by the relevant authority. This provides a significant obstacle to the proliferation of UAS, as deployments are reviewed largely on a case-by-case basis by way of the SORA.

Regulatory progress towards a quantitative ground risk model is being made by the Joint Authorities on Rule making for Unmanned Systems (JARUS), a non governmental body providing guidance on UAS policy across many National Aviation Authorities (NAAs) with the goal of providing standardised guidance to be used by NAAs when writing their respective UAS policies and avoiding duplication of efforts.

JARUS SORA guidelines use Ground Risk Classes (GRC) to classify the unmitigated risk of a UAS striking a person, based upon basic parameters derived from the UAS operation and its maximum dimension. The model uses the concept of lethal area, which is defined as the area within which the UAS is likely to cause a fatality [5]. This calculation can broadly be separated into calculation of the lethal area of the UAS, based upon UAS characteristics, and estimation of population density of the area of impact to determine the number of people at risk of being struck as a result of the impact. It can be seen that the inclusion of a more accurate population density map for the time of the UAS operation

*PhD Student, Faculty of Engineering and the Environment, University of Southampton, Southampton, SO17 1BJ, United Kingdom

†Associate Professor, Faculty of Engineering and the Environment, University of Southampton, Southampton, SO17 1BJ, United Kingdom

‡Professor, Faculty of Engineering and the Environment, University of Southampton, Southampton, SO17 1BJ, United Kingdom

§Research Fellow, Faculty of Engineering and the Environment, University of Southampton, Southampton, SO17 1BJ, United Kingdom

would benefit this approach greatly, preventing the unnecessary restriction of UAS operations due to overestimation of the GRC. This work contributes to this with the integration of a spatiotemporal population model.

A. Related Previous Work

Numerous prior works aim to identify risk posed by UAS overflying or flying near to specific ground features and installations, with Washington et al. [6] identifying 18 different ground risk models. These ground risk models can then be combined with path finding methods to produce operational flightpath routings. A comprehensive review of ground risk models was conducted by Washington et al. [6].

1. Ground Risk Identification and Mapping

Clothier et al. [7] introduce a generic risk assessment and evaluation framework called the Barrier Bow Tie Model (BBTM) and provide a case study on its use. The BBTM is actively used in UAS safety cases submitted to the Civil Aviation Authority (CAA) in the United Kingdom. The BBTM is a conceptual framework for structuring the risk assessment with a focus on the mechanisms and relationships between aggravating and mitigating factors associated with a given hazard. These factors act as "barriers" to threats that lead to the realisation of a hazard condition as well as mitigation to any resulting consequences from the hazard condition. The generic nature of the BBTM lends it to being an overarching framework for UAS risk assessment.

Ancel et al. [8] develop a real-time risk assessment framework for integration with Uncrewed Traffic Management (UTM) concepts. This consists of an estimation of impact and casualty areas of a small UAS with subsequent estimation of potential casualties based on a local population density database. This is superimposed on a satellite image of the operational area. A conventional risk matrix, common in most generic risk assessments, is constructed by binning risk values by probability of occurrence. This can help when risk assessments are disseminated to non-technical persons, although the BBTM is still likely to be understood.

Aalmoes et al. [9] develop and implement a third party risk (TPR) model based on a prior framework by Ale et al. [10], developed for risk assessment of conventional aviation around major commercial airports. The model considers UAS accident probability, potential impact area and lethality probability.

Primatesta et al. [11] create ground risk maps incorporating some OpenStreetMap (OSM) city data for a local area of Turin, Italy. Specific data for population density in the city is not used and is replaced with an artificially generated population density map. The ground risk map is on a finer scale than the work presented in this paper, including individual buildings and estimates of sheltering factor specific to such areas from OSM data. This is allowed by the use of an artificial population density grid.

Melnyk et al. [12] use work done to estimate human exposure to environmental pollutants by Klepeis et al. [13] in order to proportionally weight population density values by expected time spent in various environments. The environments, as specified by Klepeis et al., are used to scale the local population density proportionally to the area coverage of a known environment type within the analysed area. To the best of the authors knowledge, this represents the current state of the art in temporal ground risk modelling.

Sheltering effects that account for structures at or in the vicinity of the impact site of a UAS that mitigate the person striking or lethality probability of a UAS impact are used in Ancel et al., Melnyk et al., Bertrand et al., Primatesta et al. and la-Cour Harbo [8, 11, 12, 14, 15]. The sheltering factor does not take a standard range of values and is applied with differing methodologies; it is applied as a factor in the probability of striking a person as in [15] or in the probability of a fatality given the striking of a person with a UAS [11, 14]. The value of the sheltering effects is described as a probability, $p_s \in [0, 1]$ or as a scaling factor, $S > 0$, respectively. Other works use qualitative measures of roof structural resistance to penetration by debris [8, 12]. It is important that any sheltering effects are only included once in the overall risk calculation in order not to underestimate risk. Quantitative methods are preferred and are used in this work in line with the quantitative nature of the remainder of the ground risk methodology used.

2. Ground Risk Aware Path Finding

Feyzabadi et al. [16] model the risk-aware path finding problem as a Constrained Markov Decision Process (CMDP) and evaluate the approach on simulated indoor factory environments. The authors note that CMDPs are computationally complex, therefore not suitable for dynamic environments where multiple path recomputations may be required in response to environmental changes. The authors apply a hierarchical method aggregating empty space into larger regions; this reduces the time taken to obtain a path at the cost of sub optimal path selection.

Primatesta et al.[17][18] extend the well known Rapidly expanding Random Tree (RRT*) and A* search algorithms respectively to minimise the risk value of found paths.

The latter A* based approach builds upon that considered by Guglieri et al. [19] and includes both offline and online elements of path finding, allowing refinement and recalculation of offline paths, found in a static two-dimensional risk environment, to dynamic changes. The risk aware behaviour is achieved using risk based cost and heuristic functions as part of the standard A* search procedure. A post-optimization procedure consisting of sequential line-of-sight checks to eliminate unnecessary nodes in the path is performed to improve the quality of the path as well as reducing the zigzag effect caused by use of a uniform grid environment for searching.

Sampling based approaches do not require the pre-generation of a graph for the configuration space, therefore save on this runtime cost that must be incurred by graph based algorithms. Particularly in higher dimensional spaces this could involve three dimensional triangulation, which can result in long generation times and regeneration of at least parts of the triangulation in response to configuration space changes.

B. Spatiotemporal Population Distribution

Sutton et al. [20] estimate population distributions for day and night time cases using a variety of data sources. Gridded Population of the World datasets [21] from official sources as well as satellite imagery based estimates were used for the day time case. Similarly, satellite imagery of light distribution was used to derive population estimates by using the light distribution as a mask to separate urban and rural areas, then estimate population based on the amount of stable light in a given pixel of the image given as gain. However, this approach lacked spatial resolution and was still dependent upon prior population data in order to linearly relate the amount of light for each pixel to a population density in that area.

Martin et al. [22] develop a flexible framework for spatiotemporal modelling of populations that is able to generate population distributions for any combination of spatial and temporal inputs. Estimates for dynamic populations derive from daily workflows segregated by demographic categories, for example school children or the elderly, which are mapped to their expected spatial locations for a given time. The approach is dependent upon open governmental data sources instead of externally sensed data; this work makes use of a subset of these data sources, however the extension of this work to use the entire set of data sources in Martin et al. [22] is possible.

This paper contributes to research by introducing a temporal dimension to ground risk analysis through the construction of spatiotemporal population density maps using a location agnostic methodology. The paper is structured in the following manner. Section II details the generation of the population density map including temporal variation. Section III describes the risk analysis methodology. Finally, Section IV demonstrates several example use cases for the risk maps generated and conclusions are drawn in Section V.

II. Population Density Map Generation

Past work by Primatesta et al. [11] considered artificially generated population density distributions. This work estimates actual population distributions from the highest resolution authoritative data source available, namely census data. Whilst this is likely better than a uniform value being set for population density over large areas, this approach can still result in overestimation of the risk posed in urban areas due to the loss of resolution caused by using real data. The approach presented here is therefore more suited to longer BVLOS operations outside and around urban areas. The decision to use generic national data sources instead of attempting to concatenate many local datasets, which may have offered finer detail, was made to allow the approach to have a wide spatial applicability.

This work incorporates concepts from the spatiotemporal framework defined by Martin et al [22] and initially categorises the population into residential (PR), non-residential (PNR) and transiting (PT). Each category forms a proportion of the total population at any given hour of the day, such that for any time all categories always sum to 1. These proportions are derived from the National Human Activity Patterns Survey (NHAPS) conducted by Klepeis et al [13], shown in Figure 1 and are referred to with a lowercase p ; they are termed $p_R(t)$, $p_{NR}(t)$ and $p_T(t)$ respectively for a time t .

In order to derive population densities (and absolute numbers), data from the census detailing the PR is assumed to form 100% of the available population and is referred to as the population budget $\sum P$ for a given area. This is a similar assumption to that made by Martin et al. [22] and can be justified by the census only surveying residential areas, therefore capturing the entire population. This however requires a minimum population budget to ensure the results remain representative in aggregate; this is set to 200,000.

In order to derive the population proportions at a given time, the population categories from Martin et al are mapped

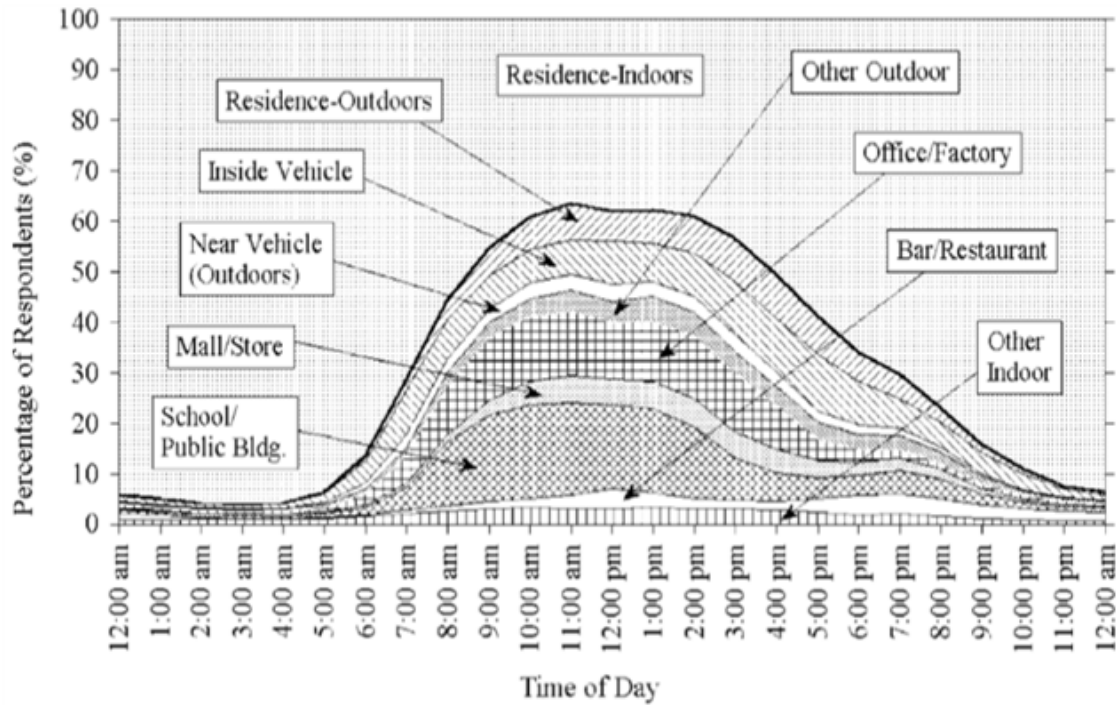


Fig. 1 Diurnal activity patterns of NHAPS respondents. Figure from [13]

to the activity locations from Klepeis et. al. This mapping is seen in Table 1. The temporal populations proportions must then be located spatially; this requires combination with geospatial geometries appropriate to the activity. For this work Open Street Maps (OSM) [23] is used. OSM stores metadata, referred to as tags, about all geospatial entities allowing for filtering of only entities with desired tags. The NHAPS activity locations are mapped to OSM tags that are used to retrieve geospatial geometries of corresponding areas. This mapping is described in Table 2. The NHAPS activities are used as a higher fidelity categorization to that of Martin et al. The transiting population is assumed to use road vehicles exclusively and is omitted from these mappings as it is handled separately with additional data.

PR	PNR	PT
Residence-Indoors	Office/Factory	Inside Vehicle
Residence-Outdoors	Bar/Restaurant	
	Near Vehicle (Outdoors)	
	Other Outdoor	
	Other Indoor	
	Mall/Store	
	School/Public Bldg.	

Table 1 Mapping of population categories to NHAPS activity locations

Further consideration is made for the PT; official road traffic statistics are used instead of an assumption of uniform density for all roads at a given time. We use the same study used by Melnyk et al. [12] (Klepeis et al. [13]) to find that an average person spends 5.5% of their day inside a vehicle, this proportion is an average value over the course of the day and is expected to be broadly divided into two journeys at the traditional morning and afternoon commuting times respectively. The same study showed that 6% of the representative sample of people surveyed were in a vehicle at 9am, rising to 9% at 3pm. Official national statistics for the United Kingdom also indicate that 68% of people commute using a form of road vehicle [24]. The accurate quantification of the vehicular traffic is therefore required to obtain an accurate estimate of spatiotemporal population density.

NHAPS Activity Locations	OSM Tag
Residence-Indoors	landuse=residential
Residence-Outdoors	
Office/Factory	landuse=industrial
Other Indoor	landuse=commercial
Near Vehicle (Outdoors)	
Other Outdoor	
School/Public Bldg.	building=school building=college building=university building=government building=civic building=public
Mall/Store	landuse=retail
Bar/Restaurant	

Table 2 Mapping of NHAPS activity locations to OSM tags

It is very likely that in urban and suburban environments a significant proportion of UAS flight will be overhead existing transport infrastructure, as these may be perceived as both lower risk areas for sustained overflight compared to private buildings and more critical infrastructure as well as preferable from a legislative and public perception point of view in terms of overflight rights on private property and the likelihood of causing a nuisance to private owners. This could further be expanded to overflight of natural features such as rivers akin to the current helicopter operation in central London.

A. Residential Population

In order to preserve the existing spatial distribution information already present from census data, special handling of the PR is required. The PR in a given area is an estimate from a combination of census data [25] [26], OSM and NHAPS data. Residential area geometries \mathbf{G} are combined with census boundary geometries \mathbf{C} to find a set of polygonal regions \mathbf{W}_R such that

$$\mathbf{W}_R = \mathbf{C} \cap \mathbf{G}$$

The set of all polygons within a layer is termed \mathbf{W}_R , with individual polygons w and

$$\rho(w_R, t) = \rho_{\max}(w_R) p_R(t)$$

is the corresponding residential population density for the polygon w_R at time t . $\rho_{\max}(w_R)$ is the maximum density of the polygon defined by census data, demonstrated in Figure 2. This effectively scales the population densities of the fully populated census areas by the proportion of population in residential areas at a given time t . This ensures the population spatial distribution remains the same compared to the census data.

The intersection procedure is necessary to find only the areas of a census ward that are inhabited, increasing the accuracy of the population density estimates.

B. Non Residential Population

Unlike PR, areas that are PNR do not have an associated ground truth population density or capacity that can be used to determine the spatial distribution of population, as in the PR case. Whilst it is possible to find building maximum occupancy data for a smaller collection of buildings [22], this approach does not scale well to larger or different areas, requiring a large amount of manual data input and subsequent updating.

We take a simplified intuitive approach similar to that described by Holt et al. [27]. The population, P_l located in NHAPS defined locations, l , is found by the product of the population proportion for those locations $p_l(t)$ at the time t

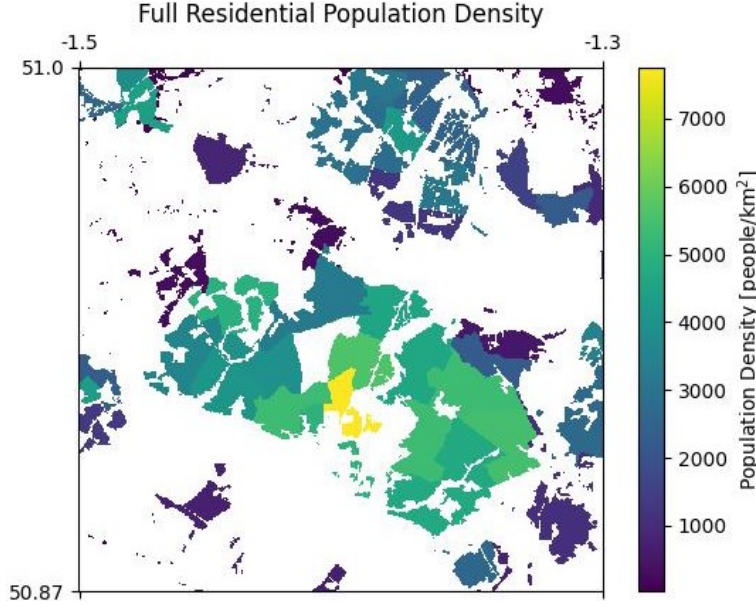


Fig. 2 Residential Population map for the Southampton area, derived directly from census data. This shows the maximum density each residential area can have, when the entire population of the mapped region is assumed to be in their homes. Here, PT and PNR are assumed to be zero and 100% of the population are PR.

and the total population budget $\sum P$

$$P_l(t) = p_l(t) \sum P$$

This population must then be distributed uniformly across all geometries that correspond to l , with the set of all such polygons termed \mathbf{W}_l

$$P(w_l, t) = P_l(t) \frac{\text{area}(w_l)}{\sum_{w \in \mathbf{W}_l} \text{area}(w)}$$

This can be simplified to a uniform population density for all w_l

$$\rho_l(t) = \frac{P_l(t)}{\sum_{w \in \mathbf{W}_l} \text{area}(w)}$$

C. Road Traffic Population

The road traffic population consists of historical road traffic and vehicle occupancy estimates. Historical road traffic is derived from open governmental data provided by the United Kingdom Department for Transport [28][29] in the form of Annual Average Daily Flow (AADF) tables. AADF tables are produced by a combination of automatic traffic counters and manual enumeration of vehicles at a given point of on the road network. The data used in this work uses the amalgamated traffic direction version, with counts categorized by vehicular type. AADF values are scaled by similarly provided values corresponding to hours of the day in order to obtain estimates for traffic flow for an average day in the year. As external data is used here, if there is conflict with the value for PT, the external data is taken as ground truth and used in place of PT estimates.

Vehicular traffic values are transformed to estimates for road traffic population in order to achieve dimensional compatibility with the residential population layer values and other layers in the model as a whole. An estimate for the occupancy of cars and taxis is made using official statistics [30], however for the remainder of the categories a plausible estimate of the occupancy of each type of vehicle detailed in the AADF data is made, shown in Table 3, however no attempt is made to justify the validity of these values. Further work could use different statistical estimates of these values for enhanced accuracy. As a preprocessing step, all traffic counter data is transformed with the use of the vehicle occupancy estimates to a single population estimate at each traffic counter location, \mathbf{T} .

Type	Estimated Occupancy
Cars&Taxis	1.6
Two-wheeled motor vehicles	1.2
Buses&Coaches	40
Pedal Cycles	1
Light Goods Vehicles	1.5
Heavy Goods Vehicles	1.6

Table 3 Estimated Occupancy of different vehicle types

As traffic counter data is spread relatively sparsely on the road traffic network, interpolation of values must be performed considering the actual geometry of the roads. Similarly provided data specifying the geometry of the road network is obtained in ESRI shapefile format. A novel road traffic interpolation algorithm is proposed in Algorithm 1.

Input: unique road identifiers L ; road geometry line segments S ; traffic counter populations T ; interpolation resolution r ;

Result: a set of 2-tuples of georeferenced polygons and associated population density values P

for $\forall l \in L$ **do**

$S_l \leftarrow \text{GetSegmentsForRoad}(S, l)$

$T_l \leftarrow \text{GetCountersForRoad}(T, l)$

$O \leftarrow$

for $\forall s \in S_l$ **do**

$T_s \leftarrow \text{GetCounterForSegment}(T_l, s)$

 carriedLength := 0

if $T_s \neq$ **then**

$O \leftarrow O < (\text{length}(s) + \text{carriedLength})$

 carriedLength := 0

else

end

 carriedLength += length(s)

end

 nPoints $\leftarrow \lfloor \max(O)/r \rfloor$

$M_l \leftarrow \text{Interpolate}(O, T_l, nPoints)$

$w \leftarrow \text{GetRoadWidth}(l)$

$R_l \leftarrow \text{Buffer}(S_l, w)$

for $\forall i \in \{0, 1, 2, \dots, nPoints\}$ **do**

 clippedPolygon $\leftarrow \text{Buffer}(\text{GetLatLng}(O_i), r/2) \cap R_l$

$P \leftarrow P < \{\text{clippedPolygon}, M_{l,i}/\text{area}(\text{clippedPolygon})\}$

end

end

Algorithm 1: Interpolation of road traffic counts

Algorithm 1 is based on the projection of each road geometry to a single dimension then combination of existing traffic counter locations and their population values. Some road segments do not have an associated counter, we check for this on Line 7. These segments must therefore have their length carried forwards to the next segment which does have a counter, as in Line 12.

The interpolation resolution, r , is defined as the maximum distance in metres between consecutive interpolated locations on the same road and is constrained to be less than the resolution of the map raster grid to prevent continuous road geometries having gaps due to insufficient sampling along their length. This value is used to calculate the quantity of intermediate points that interpolation must be performed for on Line 15. Linear interpolation is performed using the true ordinate and population values on Line 16.

The road geometry is recovered by using sequence of geometric buffering and intersection. Each interpolated point

is buffered by half the road interpolation resolution to cover the length of the road between interpolation points on Line 20. This can result in the buffered polygon extending further than the road width therefore, the intersection with the actual width of the road is used instead. The road width is found from the same data sources as the road data itself.

Population density is estimated by dividing the interpolated population by the area of the polygon, fixed at rw .

Figure 3 demonstrates the large temporal variation in road population density for the same area at different times. This is calculated using Algorithm 1.

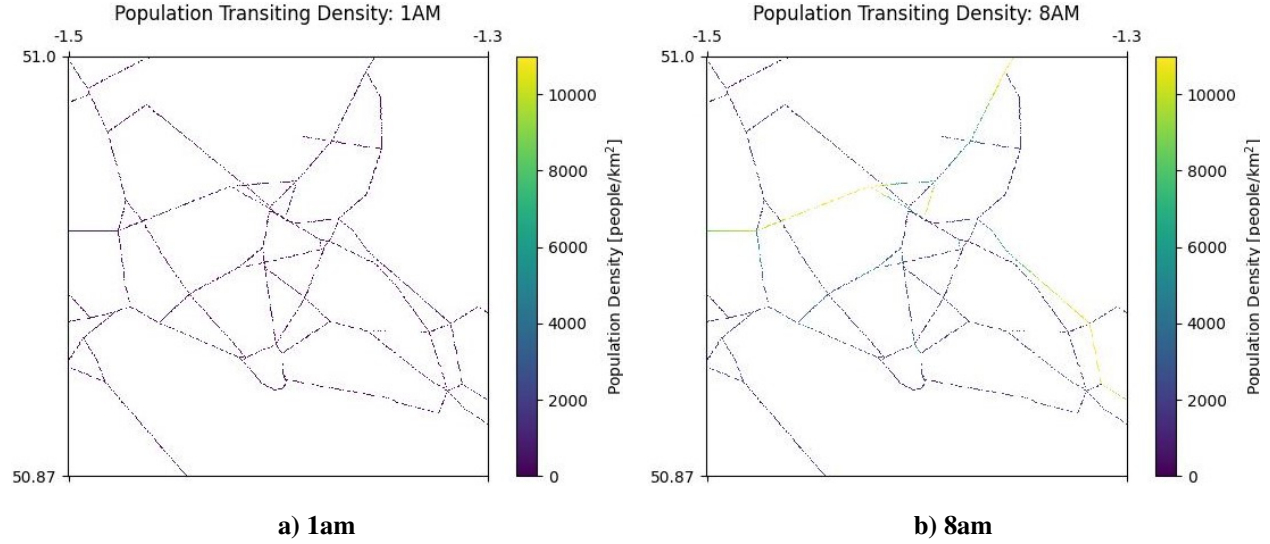


Fig. 3 Roads population density at different times around Southampton, UK. Left is a quiet period during the night, right is a "rush hour" traffic period.

D. Map Layering

As illustrated in Figure 4, the population map is composed of a number of geospatial layers that are overlaid to form the final map. Layers are further subdivided by functionality into data layers or annotation layers, with the former allowing for external data to be processed and displayed. Annotation layers are granted access to composited data layers and the aggregated data used by each of the data layers, using which further information can be displayed on the map. Annotation layers are not permitted access to external data.

Population density estimate data layers, \mathbf{P} consist of population density estimates with aggregation for n layers performed by

$$\mathbf{P}_{\text{Agg}} = \sum_{i=0}^n \mathbf{P}_i$$

Blocking layers, \mathbf{B} , represent geometries over which overflight is prohibited. This is represented by

$$\mathbf{B}(x, y) = \begin{cases} -1 & \text{if overflight prohibited} \\ 0 & \text{otherwise} \end{cases}$$

where x, y represent the raster grid pixel location. They are aggregated similarly as such

$$\mathbf{B}_{\text{Agg}} = \sum_{i=0}^n \mathbf{B}_i$$

As population estimates are not required for regions that are marked as blocked, the population estimates, \mathbf{P}_{Agg} , and blocking, \mathbf{B}_{Agg} , layers are aggregated into a single data layer, \mathbf{D}_{Agg} , similarly to above

$$\mathbf{D}_{\text{Agg}}(x, y) = \begin{cases} -1 & \mathbf{B}_{\text{Agg}}(x, y) \leq -1 \\ \mathbf{P}_{\text{Agg}}(x, y) & \text{otherwise} \end{cases}$$

Blocking layers are based on the same GIS data that is used to construct the geometry of any other layers.

Annotation layers are treated differently to other layers in that they are not aggregated element-wise. Instead a transparency mask is applied to all annotation layers, which are overlaid without operating on any geometries within layers. The initial overlay ordering is first-come-first-served, based on layer generation time. Finally, the aggregated annotations layer, \mathbf{A}_{Agg} , is overlaid on the aggregated data layer, \mathbf{D}_{Agg} , to form the final map, \mathbf{R} .

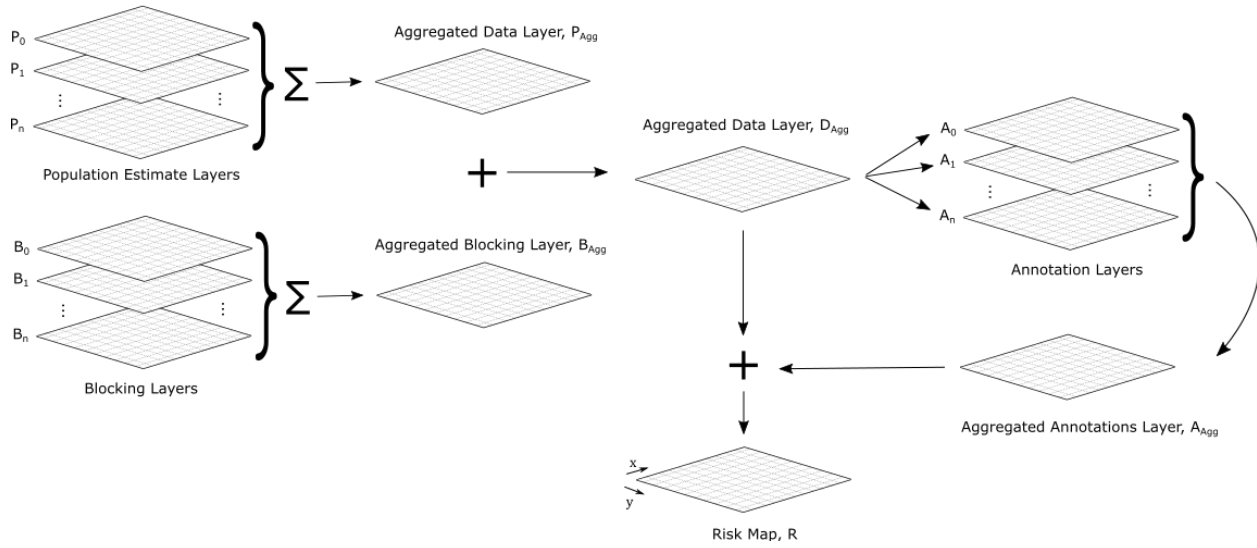


Fig. 4 Map Generation Model

III. Flight Path Ground Risk Analysis

The probabilistic approach taken to analyse the risk posed to people on the ground by a UAS is widely used in previous work [7, 11, 15]. It is based on the sequential occurrence of independent events, each with associated probabilities. The events, in order of occurrence, are:

- 1) Loss of Control (LoC) event that results in the UAS impacting the ground
- 2) Striking a person(s) as a result of the uncontrolled descent
- 3) The struck person(s) being fatally injured as a result

We extend previous models with the addition of time based quantities

$$P_{casualty}(x, y, t) = P_{LoC} \cdot P_{strike}(x, y, t) \cdot P_{fatality}(x, y)$$

where x, y refer to the spatial dimensions, t is hour of the day. The hour of the day t is used to as input to the spatiotemporal population density model.

A. Uncontrolled Descent Events

The types of uncontrolled descent considered are a subset of those considered by Primatesta et al [11] and share similar methodologies.

1. Ballistic Descent

Under ballistic descent the UAS is assumed to be a projectile producing no useful lift, therefore the predominant forces acting upon it become aerodynamic drag and gravity. The second order drag model developed by la Cour-Harbo [15] is used to model this. This model provides one dimensional results for distance and time between the LoC event and ground impact and the velocity and angle of the impact, the model outputs are referred to as being in the Track-Aligned Event (TAE) frame.

A ground impact probability density function (PDF) is found by randomly sampling the distributions of the input variables and generating output distributions of the model outputs. As the distributions are in the TAE frame, they are rotated to the North-East-Down (NED) frame of the risk map and the effect of wind in the form of the wind vector in the NED frame

$${}^{NED}\vec{W} = \begin{bmatrix} {}^{NED}v_x \\ {}^{NED}v_y \end{bmatrix}$$

is applied the time to impact. This is translated to the location of the UAS in the NED frame

$${}^{NED}\vec{P} = \begin{bmatrix} {}^{NED}p_x \\ {}^{NED}p_y \end{bmatrix}$$

For a single sample, the impact location in the NED frame is found by

$$\begin{bmatrix} {}^{NED}x_i \\ {}^{NED}y_i \end{bmatrix} = \mathbf{R}(\theta) \times \begin{bmatrix} {}^{TAE}x_i \\ 0 \end{bmatrix} + t_i \cdot {}^{NED}\vec{W} + {}^{NED}\vec{P} \quad (1)$$

where \mathbf{R} is the usual 2D rotation matrix for the angle θ . This process is repeated for a random sample of 3000 points from each of the input distributions.

This methodology diverges from previous works in the simplification of the output sampling distribution for impact distance to the defining parameters of a bivariate distribution by fitting a bivariate Gaussian distribution to the output of this step. This reduces the PDF to its parameters with minimal loss of resolution. This is done to reduce the computational time required, particularly when generating large risk maps.

Both approaches are investigated with representative input distributions used as a case study, the bivariate impact distance PDF is generated then copied. The copy is reduced to its parameters then an equivalent number of distinct random samples are taken from this new distribution and compared with the original generated data using the correlation distance (CD). CD is a commonly used metric to compare similarity between two sample sets and is bounded $\in [0, 1]$, where 0 indicates no correlation and 1 is a perfect correlation.

An example case from Primatesta et al [11] is used, namely the Talon aircraft under ballistic descent, as the probabilistic input parameter set. The simplified result from using the proposed methodology compared to the full

unsimplified version with identical parameters is seen in Figure 5. The CD value between full and simplified PDFs was found to be 0.998 after 1000 runs of each with 3000 samples of the input distributions. This strongly supports the validity of the simplification made.

This simplification allows considerably faster computation as segments of the path with the same UAS track angle only require the relatively very fast translation step from TAE to NED frames as the covariance matrix of the PDF remains the same for the same UAS track. This allows the computation of the ground risk at every point with a reasonable computational speed.

A Gaussian Kernel Density Estimation (KDE) approach was also tried, however this yielded poor computational performance, at times slower than that of the full calculation due to the non parametric nature of KDE resulting in the performance decreasing with increasing sample size.

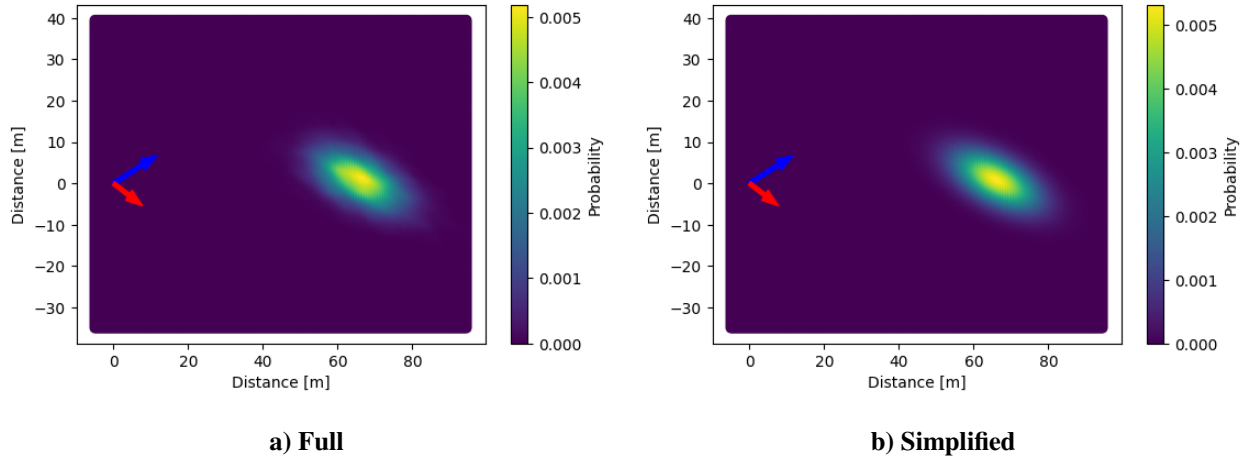


Fig. 5 Comparison of ballistic descent PDF in the NED frame for the Talon aircraft in Primatosta et al. [11]. The parameters used are detailed in Primatosta et al. The left panel shows a recreated plot while the right shows the result of applying the proposed simplification method. The blue arrow represents the UAS velocity and the red arrow represents the wind velocity vector. This demonstrates the similarity of the simplified method to the original.

2. Uncontrolled Glide

A simple model of gliding flight is used for determination of glide distance d_{impact} and time t_{impact} assuming a best gliding speed of V_{BG} and glide ratio γ

$$d_{impact} = \gamma h \quad (2)$$

$$t_{impact} = \frac{d_{impact}}{V_{BG}} \quad (3)$$

Wind effects are applied as previously described.

B. Probability of Striking Persons

The probability of striking a person, P_{strike} , given an the impact of a UAS at a position x, y and time t is

$$P_{strike}(x, y, t) = \sum PDF \cdot \rho(x, y, t) \cdot A_{exp}(\theta) \quad (4)$$

where ρ is the population density, A_{exp} is the lethal critical area. The population density is as aggregated into the \mathbf{P}_{Agg} layer of the map. The critical area is the projected area on the ground that is exposed to the impact and is found using the common approach by Smith [31] used in [8, 9, 11, 14].

C. Probability of Fatality

The fatality model used here was proposed by Dalamagkidis et al. [32] and is based upon a logistic growth model as shown in Figure 6. The curve is defined by

$$P_{\text{fatality}}(x, y) = \frac{1}{1 + \sqrt{\frac{\alpha}{\beta}} \left[\frac{\beta}{E_K^{\text{imp}}(x, y)} \right]^{\frac{1}{S(x, y)}}} \quad (5)$$

where $E_K^{\text{imp}}(x, y)$ is the impact kinetic energy, α is the impact energy required for 50% probability of fatality at a shelter factor $S = 0.5$ and β is minimum impact energy to cause a fatality with no shelter ($S \rightarrow 0$). In this work, the shelter factor is assumed to be 0.3.

The shelter factor $S(x, y)$ encompasses shelter effects that obstacles in the vicinity of the impact have both in terms of blocking the path of the UAS, resulting in it not striking a person and absorbing impact energy.

The shelter factor can be applied at the stage of finding the probability of striking a person [11, 33] or at the stage of calculating the fatality probability [14, 15]. The former approach is adopted in this work. The application of shelter factor at the fatality calculation stage functions as both an "impact energy absorption factor" and "deflection probability" factor. Regardless of approach taken, sheltering effects must only be included once in the final calculation to ensure the risk is not underestimated.

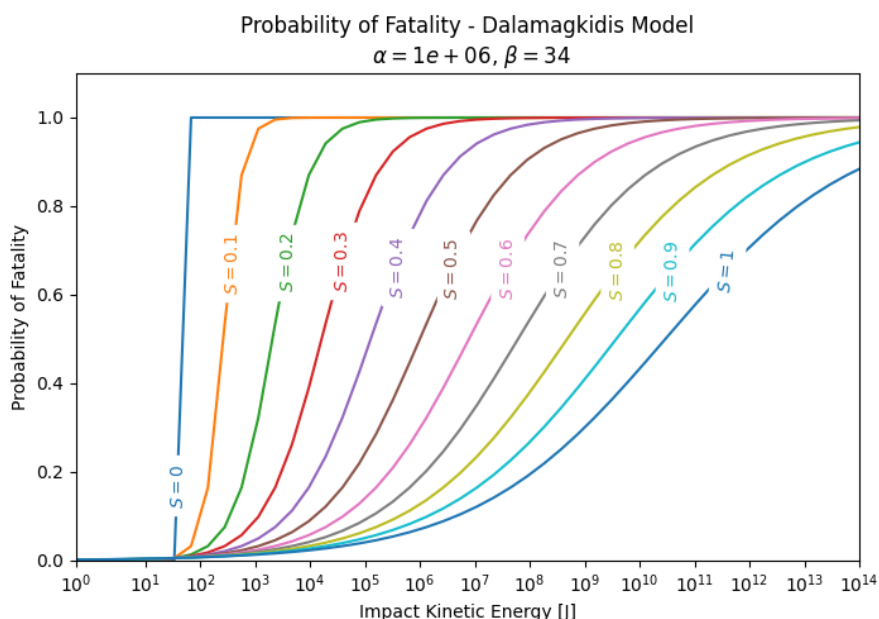


Fig. 6 Fatality Curves created from the model by Dalamagkidis et al. [32]

IV. Results and Discussion

A. Implementation

The tool is implemented in Python [34] using common geospatial and data science libraries[35][36]. The Casualty Expectation toolbox is also used [37]. The visualization and the user interface are based on the Holoviews[38][39] and PySide2 Qt libraries respectively.

Geometries are obtained in the EPSG:4326 coordinate reference system (CRS), also known as the WGS84 CRS and is used by the Global Positioning System (GPS) constellation. EPSG:4326 is unsuitable for calculation of geometric properties as degrees are used as the unit of measurement (UoM) and it does not preserve areas. In order to calculate areas, a projection with a UoM in metres must be employed. This is selected as EPSG:3395, which is suitable for small scale mapping and, crucially, preserves true areas. Geometries are first copied and projected to EPSG:3395 before any

geometric operations are performed. This mitigates the projection distortion effects discussed by la Cour-Harbo [15], as all geometric calculations are performed in the EPSG:3395 CRS and the common EPSG:4326 CRS is used only for input and output of data as well as visualisation.

Specifically for the population density census data, the UK 2011 (currently the latest available) census data aggregated into output areas (OA) is used. A clipped version of the OA boundaries is used that does not include bodies of water. This is to ensure that the population is not underestimated by a larger area despite areas that are uninhabitable due to water. OAs form the smallest unit of resolution within the census dataset and are required to aggregate a minimum of 40 residential households or 100 residential people largely for privacy reasons. This has been chosen to provide the highest spatial resolution possible, however the method presented in this work is equally valid for larger areas such as the super output areas (SOAs). This could be necessary in areas where the data is not available to the same spatial resolution as other OAs.

A further advantage of using OAs is the division of urban and rural areas created when forming the boundaries, where possible[40]. Urban and rural areas have differing ground risk characteristics, largely due to the difference in population density and infrastructure, therefore their division results in more uniform individual OAs compared to the mixed urban rural case.

B. Population Density Maps



Fig. 7 Southampton region used throughout this paper for demonstration. The mouth of two rivers joins at the southern tip of the city with the majority of the waterfront consisting of docks. There is a shopping centre north of the tip and a large park in the centre of the city.

A region encompassing Southampton, UK is used as an example; a satellite view of the region is seen in Figure 7. The upper right of this view also shows Southampton Airport which is only considered later through the addition of the corresponding Flight Restriction Zone for UAS around it.

The population density maps generated demonstrate a marked redistribution of population throughout the day with residential areas almost regaining their full populations as defined in the census data during night time hours, shown in Figure 2. Daylight hours demonstrate a shift toward industrial, commercial, public and retail areas as people relocate to workplaces and engage in commerce. These effects are seen in Figure 8.

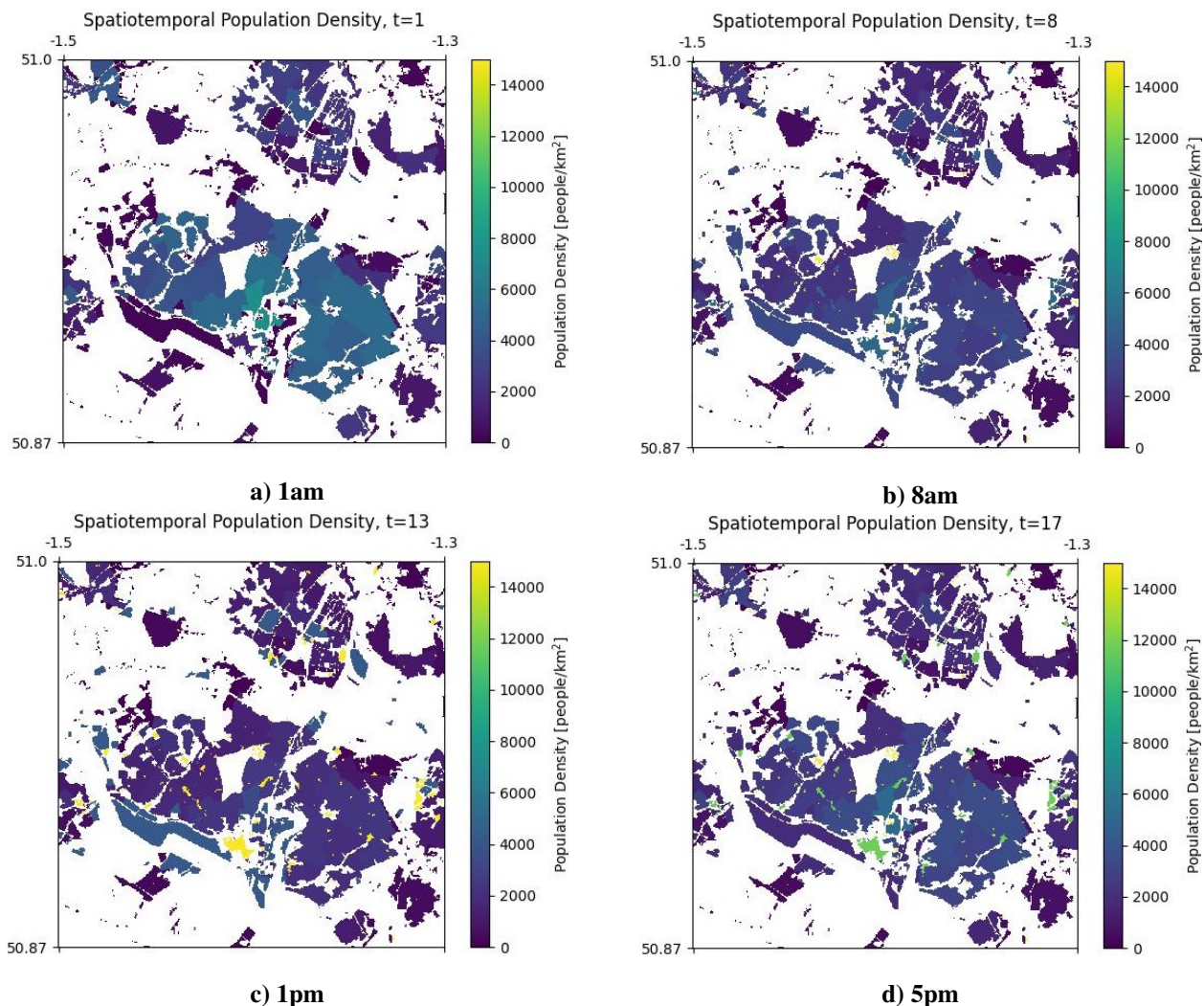


Fig. 8 Comparison of static populations at different times of the day around Southampton, UK. All bounding coordinates are in decimal degrees.

It is seen that the population density of industrial areas such as the docks is much lower outside of conventional work hours therefore would carry much lower overflight risk during night time hours. Particularly noticeable on the 1pm population density map are the high population densities associated with schools, hospitals and public buildings, which appear as bright yellow points; these areas have previously been suggested as being marked as no fly zones, however the spatiotemporal analysis of ground risk presented here would exclude this possibility regardless of the presence of a no fly zone if a form of route risk optimisation is used to find a route minimising cumulative risk value. This greatly simplifies the planning phase of UAS operation, where the holistic approach taken here eliminates the requirement for individual locations such as schools or hospitals to be firstly identified in a proposed UAS operation area and subsequently avoided manually; they would be automatically included in the risk map and avoided, subject to their level of risk, by a suitable path planning algorithm.

The blank area in the centre of Figure 8 corresponds to the large park in the centre of the city shown in Figure 7. Any population in this area are not accounted for in this model, as there are no available datasets for deriving the population distribution in such areas. There is potential for a mobile phone based approach to determining spatiotemporal population distribution in any area with sufficient cell network coverage. This is explored for areas in Portugal and France by Deville et al. [41], however, the acquisition of such datasets is problematic in terms of privacy and public relations implications. Provided these barriers could be overcome, it is foreseeable that a real time data feed could be used to generate tactical risk maps and reroute UAS as required.

C. Risk Map Temporal Variation



Fig. 9 The Swoop Aero aircraft used as an example for generating risk maps. Image from [42]

Parameter	Value
Mass [kg]	17
Length[m]	1.63
Width[m]	2.22
Horizontal Airspeed [m/s]	31
Frontal Area [m ²]	0.5
Ballistic Descent Drag Coefficient	0.8
Glide Airspeed [m/s]	21
Glide Ratio	11
Event Probability [h ⁻¹]	5x10 ⁻³

Table 4 Parameters of the Swoop Aero aircraft used as an example.

The Swoop Aero aircraft (pictured in Figure 9) is used as an example to demonstrate the variation in the risk map at differing times. The Swoop Aero is a small fixed wing vertical takeoff and landing (VTOL) UAS, suitable for the transportation of small payloads as part of a logistics operation. The aircraft is currently utilized as part of medical logistics trials in the United Kingdom for the National Health Service (NHS) where it is transporting patient samples and medicines between hospital helipads. As mentioned previously, hospitals are can be located in and around dense residential areas, therefore it is crucial to analyze and quantify the risk posed by such medical logistics operations prior to scaling them up, particularly as some medical cargoes are classified as dangerous goods, hence are regulated more stringently [43].

The parameters used to represent the aircraft are detailed in Table 4. Only a single aircraft is used as this example demonstrates the variation in risk due to changes in time and population density, not aircraft parameters. Such relationships are explored by Primatesta et al. [11] and la Cour-Harbo [15].

Figures 10 and 11 demonstrate the person striking and fatality risk maps differing with time. Figure 12 shows the flight path used to generate the time-dependent path risk analysis show in Figure 13. In this example, the path does not change with times of the day in order to show the risk variation solely as a result of the differing time of flight, although it is foreseeable that different routes may be generated given the differing risk maps as input. The maximum risk values for each point along the path are shown in Figure 13, demonstrating the difference in risk caused by flying at a different time of the day.

This can be used by the UAS operator to schedule the operation time to reduce the ground risk. This is particularly useful in marginal cases where heavier payloads would not achieve the required ELoS, but scheduling the flight for a different time of the day would make the operation permissible, achieving the ELoS constraint.

This has implications for UAS logistics networks which in some cases would pose lower ground risk when delivering to residential locations during the middle of the day compared to before or after traditional work hours of 9am-5pm as a

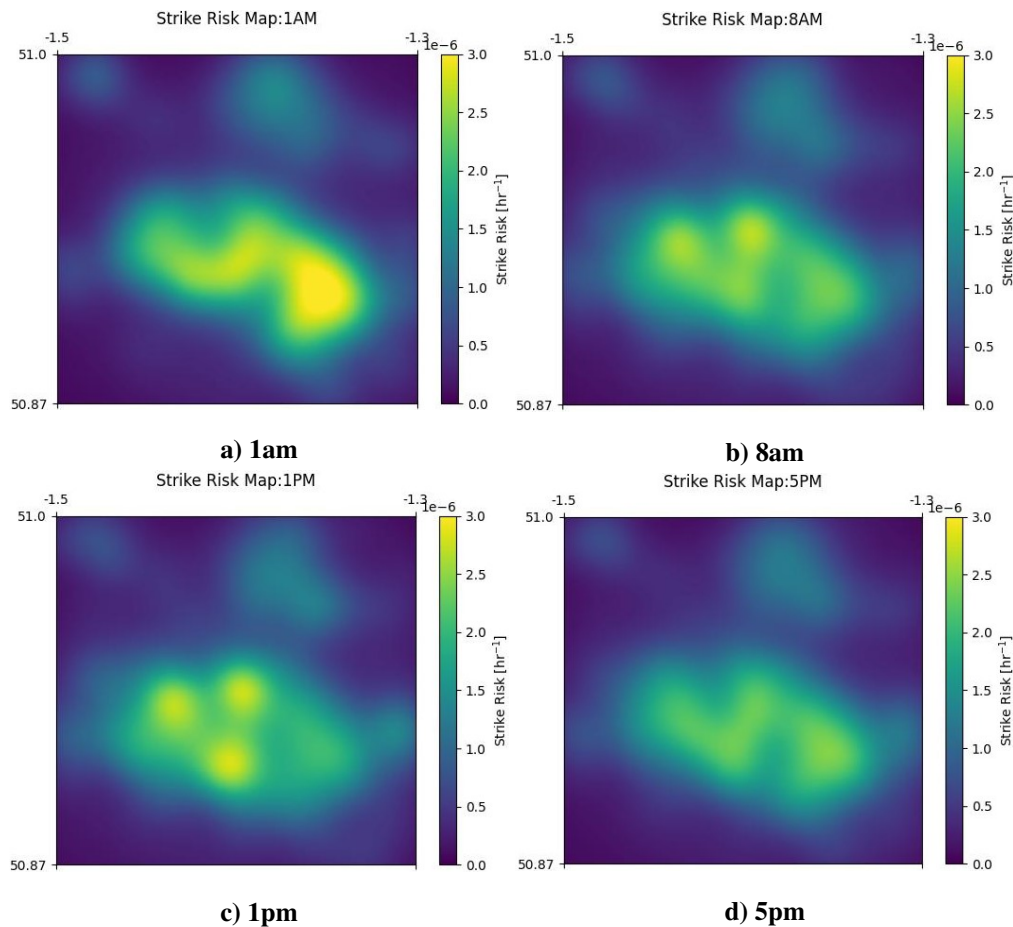


Fig. 10 Comparison of strike risk maps at different times of the day around Southampton, UK. for the Swoop Aero aircraft. All bounding coordinates are in decimal degrees.

result of more people being located outside of residential areas during these hours. This conclusion would also apply to other amenities that are usually in the vicinity of residential areas such as hospitals, although there are other considerations for such logistics networks. For example, noise levels would be increased over residential areas which may be unacceptable. UAS are also more noticeable and therefore more likely to cause a visual nuisance during daylight hours.

D. No Fly Zones

Figure 14 demonstrates the addition of no fly zones to the risk map, illustrating areas where overflight is prohibited due to Flight Restriction Zones (FRZs), usually located around airports in the UK with extended centre lines that introduce an additional buffer between UAS and approaching or departing manned aircraft. These areas are represented as values of infinity at the risk map pixel values.

No fly zones can be defined by Air Navigation Service Providers (ANSPs), either through permanent alterations to airspace or airspace classification or temporary changes through Notices to Airmen (NOTAMs) or Temporary Danger Areas (TDAs). Currently in the United Kingdom, large scale UAS operations require the establishment of a TDA which grants exclusive use of the TDA volume to the UAS operation that requested it.

No fly zones may also be established around areas such as bird sanctuaries to reduce bird strike probability and for nature preservation. There exist High Intensity Radio Transmission Areas (HIRTAs) that are marked on conventional airspace maps, that should likely be avoided by UAS as such electromagnetic emissions could cause interference with UAS Command and Control (C2) functionality, thereby increasing the ground risk around such areas, however inclusion of such effects is beyond the scope of this paper. Further permanent no fly areas are established for exclusive military use, either for the protection of aircraft from projectiles, other military aircraft or for reasons of security.

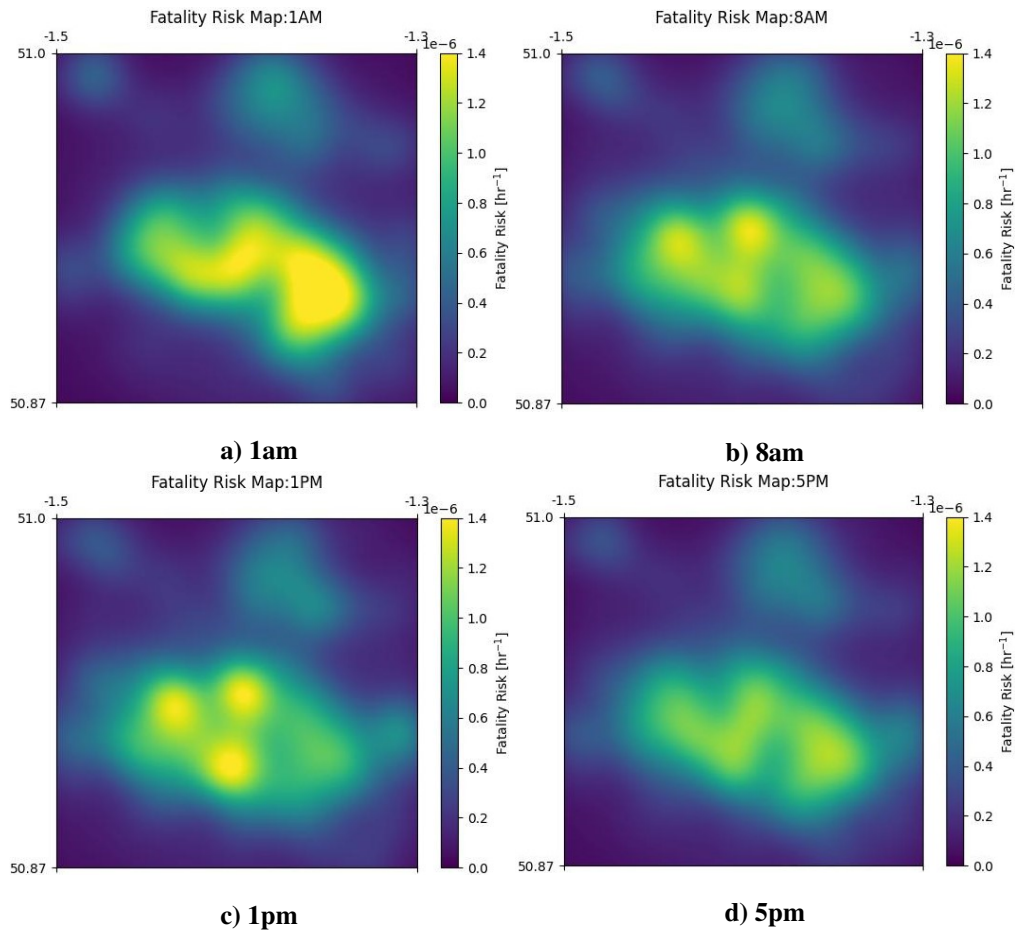


Fig. 11 Comparison of fatality risk maps at different times of the day around Southampton, UK for the Swoop Aero aircraft. All bounding coordinates are in decimal degrees.

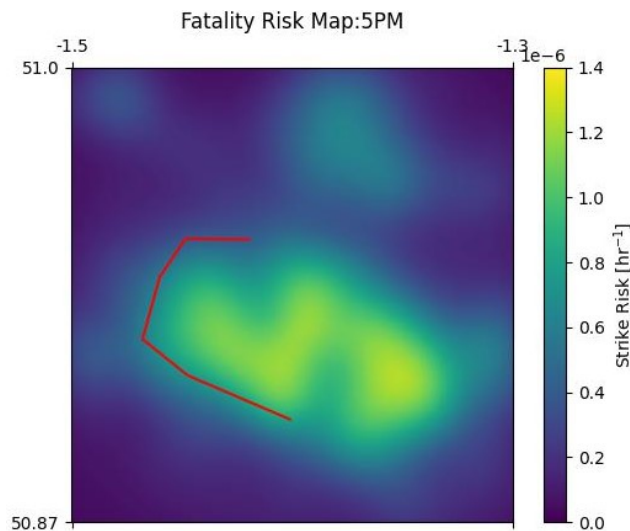


Fig. 12 Path used for analysis of temporal risk variation. The path is held constant for all times to demonstrate the effects of varying the time.

E. Discussion

The results presented demonstrate the generation of realistic ground risk maps based upon spatiotemporal population density maps. The spatiotemporal population maps are generated through a combination of governmental and open source demographic and geospatial datasets that are combined with diurnal human activity patterns from literature. This broadly accounts for a majority of the population, assuming single fixed residential and workplace locations respectively. The ground risk maps generated using this approach have potential for operational use in all stages of UAS operation.

In the regulatory approval process, prior to the operation, the quantification of ground risk allows for a concrete criteria to be established by national aviation authorities specifying acceptable quantitative levels of risk for UAS operations. Some work has been done towards this with the Ground Risk Classes established by JARUS in the SORA methodology. The validation and approval process for Operating Safety Cases that adopt a standardized, quantitative method of ground risk analysis will be reduced in both time and workload for UAS operators and regulators.

Prior to deployment, strategic decisions can be made by operators regarding the time at which the sortie(s) can take place, as well as setting sortie endpoints in lower ground risk areas, if they are not fixed. Paths can then be found that minimize the ground risk for the given set of endpoints and sortie time.

Just prior and during the sortie(s), tactical alterations to the flight trajectory can be made to minimise the risk. The efficacy of such alterations would be greatly enhanced by the integration of real time population density data as discussed later.

The approach in this work is highly extensible owing to the leveraging of OSM data. OSM provides a wealth of geographic feature tags to be used in isolation or in combination with external data to refine the map considering further factors, not necessarily directly associated with population. Obstacles such as military establishments or Sites of Scientific Special Interest (SSSI) areas can be derived for example.

The use of census data does not affect the location agnosticism of the method as it is reasonable to assume a country has performed a census. As a result of considerable time periods between census datasets, use of historical data may introduce population errors. There exist methods to interpolate and forecast intercensal data [44] which can reduce this error, although these have not been used in this work.

Further refinement can integrate real time road traffic estimates such as those used in most well known mapping and road navigation applications. Maps generated with this real time data have the potential to be used just prior to or during UAS deployment in order to inform real time operator decision making and allow them to further reduce operational risk during the course of operations. Further advancements could be made by dynamically rerouting UAS around newly found aggregations of people, in a similar fashion to current road navigation applications. Sudden aggregations could include road traffic queues for example. This is a potential functionality that could be integrated into UTM services, should they be available.

Overflight of a large number of stationary vehicles on an arterial road are foreseeable, particularly during "rush hour". In such scenarios it may be advantageous, in terms of risk posed by UAS overflight, to route over alternative areas.

A limitation of this work is the application of a constant assumed shelter factor over larger areas, the methodology is intentionally overly cautious. This can be refined by the inclusion of further data and layers to the map that would divide the larger polygons into more localized and similar areas in terms of shelter factor.

Currently, validation of the generated maps is very difficult and no attempt is made at validation beyond face validity, verifying the map matches what one would expect given the input data. This difficulty stems from the lack of either corroborating or refuting data sources from which the generation of a similar map could occur, allowing comparison and validation.

Additional difficulties are encountered in the selection and use of data sources in that more detailed data sources that include spatiotemporal data tend to only be applicable for smaller spatial regions. This is usually a symptom of the differing ownership of the data itself, with local governmental authorities collecting detailed data only for their areas of responsibility. Data sets which cover larger or national areas can be formed from aggregation and generalisation of these spatially smaller datasets, resulting in loss of effective data resolution. This forces temporal data to largely derived or inferred from such sources.

V. Conclusion

In this paper, we propose the use of spatiotemporal population density data in the analysis of ground risk posed by UAS operations. The spatiotemporal population density map is created through the combination of authoritative data sources and past works to dynamically classify proportions of a population to their expected daily activities based upon a given time. This is mapped to geospatial entities allowing for the assignment of populations to geographic locations and the subsequent calculation of the population density of these areas, in aggregate forming a population density map specific to the given time.

The population density map is used as input, together with a given flight path that can be automatically generated, to a parametric ground risk model. The model allows for the analysis of ground risk along the path in terms of risk to life per hour of operation; a conventional unit of risk in aviation. This provides UAS operators and regulators with an enhanced awareness of the ground risk posed by UAS operations in quantitative terms.

The spatiotemporal aspect of this work allows for this analysis to be performed at different times, allowing for the further reduction of ground risk posed by selecting not only lower risk routings but lower risk times of the day to fly.

To the authors' best knowledge, this is the first use of spatiotemporal data for the determination of time specific ground risk, past works have assumed notional reductions in risk at night compared to day time hours. This work analyzes the variation of risk in both spatial and temporal dimensions.

A tool is developed and open sourced [45] to encourage and promote the safety through wider use of this and as well as similar tools that aid the safe operation of UAS.

A. Future Work

Future work should focus on the acquisition and integration of further spatiotemporal data sources.

There is previous work estimating spatiotemporal population density in the vicinity of cell towers based on mobile phone data from French and Portuguese cell service providers [41]. Obtaining such data has privacy concerns, therefore the majority of providers are unwilling to release their equivalent data sets. Such a method of determining spatiotemporal population density has drawbacks if not all cell service providers are willing to participate, as it is not necessarily true that each providers data is representative of the population as a whole, neglecting those that do not have a mobile phone.

Similar dynamic prediction for road traffic has been proposed using social media data from the preceding evening [46]. The number of new methodologies based on data mining techniques is likely to continue increasing.

Further integration of real time data feeds should be considered, such as Rail data. Bertrand et al. [14] consider static ground risk assessment in the vicinity of railway tracks, neglecting the risk posed to trains themselves. This is subjectively considered to contribute less to the overall ground risk as trains are located on the rails considerably more sparsely than vehicles on a road.

Additionally, LoC event probability may be variable throughout the flight, for example during periods of higher thrust resulting in higher structural loads. This is supported by recent statistical analysis of manned aviation accidents [47] that find that 12% and 53% of fatal commercial aviation accidents have occurred during the takeoff and landing phases of flight respectively, despite being considerably smaller proportions of the total flight time at 6% and 41% respectively of an average 1.5 hour flight. This is compared to the cruise phase which is 57% of flight time and 11% of fatal accidents occurring during cruise. There are no similar statistics for UAS, however it is reasonable to assume a similar distribution of failure risk along the course of the flight, as these phases of flight are similarly critical in UAS as they are in manned aircraft. Takeoff places higher loads upon both the propulsion system(s) and the airframe, whereas landing requires precise guidance, navigation and control with increasing the risk of a LoC event should they be inaccurate or inoperative.

Acknowledgments

This work is funded by the Engineering and Physical Sciences Research Council as part of the E-Drone project under grant number EP/V002619/1.

References

- [1] "CAP 722: Unmanned Aircraft System Operations in UK Airspace - Guidance," 2020. URL <http://publicapps.caa.co.uk/modalapplication.aspx?appid=11&mode=detail&id=415>.
- [2] EUROCONTROL, "SESAR Concept of Operations for U-Space," 2019. URL <https://www.sesarju.eu/node/3411>.
- [3] EUROCONTROL, "European ATM Master Plan: Roadmap for the Safe Integration of Drones into All Classes of Airspace," 2017. URL <https://www.sesarju.eu/sites/default/files/documents/reports/European%20ATM%20Master%20Plan%20Drone%20roadmap.pdf>.
- [4] "Commission Implementing Regulation (EU) 2019/947 of 24 May 2019 on the Rules and Procedures for the Operation of Unmanned Aircraft (Text with EEA Relevance.)," 2019. URL http://data.europa.eu/eli/reg_impl/2019/947/oj/eng.
- [5] Myers, K. A., "LETHAL AREA DESCRIPTION:," 1963. <https://doi.org/10.21236/AD0612041>, URL <http://www.dtic.mil/docs/citations/AD0612041>.
- [6] Washington, A., Clothier, R. A., and Silva, J., "A Review of Unmanned Aircraft System Ground Risk Models," Vol. 95, 2017, pp. 24–44. <https://doi.org/10/gct2hz>, URL <http://www.sciencedirect.com/science/article/pii/S0376042117301392>.
- [7] Clothier, R. A., Williams, B. P., and Hayhurst, K. J., "Modelling the Risks Remotely Piloted Aircraft Pose to People on the Ground," Vol. 101, 2018, pp. 33–47. <https://doi.org/10/gcqh5>, URL <http://www.sciencedirect.com/science/article/pii/S0925753516306427>.
- [8] Ancel, E., Capristan, F. M., Foster, J. V., and Condotta, R. C., "Real-Time Risk Assessment Framework for Unmanned Aircraft System (UAS) Traffic Management (UTM)," *17th AIAA Aviation Technology, Integration, and Operations Conference*, American Institute of Aeronautics and Astronautics, 2017. <https://doi.org/10.2514/6.2017-3273>, URL <https://arc.aiaa.org/doi/abs/10.2514/6.2017-3273>.
- [9] Aalmoes, R., Cheung, Y. S., Sunil, E., Hoekstra, J. M., and Bussink, F., "A Conceptual Third Party Risk Model for Personal and Unmanned Aerial Vehicles," *2015 International Conference on Unmanned Aircraft Systems (ICUAS)*, 2015, pp. 1301–1309. <https://doi.org/10/ghs9n8>.
- [10] Ale, B. J., and Piers, M., "The Assessment and Management of Third Party Risk around a Major Airport," Vol. 71, No. 1-3, 2000, pp. 1–16. <https://doi.org/10/ffrnz5>.
- [11] Primatesta, S., Rizzo, A., and family=Cour Harbo, p. u., given=Anders, "Ground Risk Map for Unmanned Aircraft in Urban Environments," Vol. 97, 2020. <https://doi.org/10/ghs9pf>.
- [12] Melnyk, R., Schrage, D., Volovoi, V., and Jimenez, H., "A Third-Party Casualty Risk Model for Unmanned Aircraft System Operations," Vol. 124, 2014, pp. 105–116. <https://doi.org/10/ghs9pb>, URL <http://www.sciencedirect.com/science/article/pii/S095183201300313X>.
- [13] Klepeis, N. E., Nelson, W. C., Ott, W. R., Robinson, J. P., Tsang, A. M., Switzer, P., Behar, J. V., Hern, S. C., and Engelmann, W. H., "The National Human Activity Pattern Survey (NHAPS): A Resource for Assessing Exposure to Environmental Pollutants," Vol. 11, No. 3, 2001, pp. 231–252. <https://doi.org/10/fjw2rt>, URL <https://www.nature.com/articles/7500165>.
- [14] Bertrand, S., Raballand, N., Viguiet, F., and Muller, F., "Ground Risk Assessment for Long-Range Inspection Missions of Railways by UAVs," *2017 International Conference on Unmanned Aircraft Systems (ICUAS)*, 2017, pp. 1343–1351. <https://doi.org/10/ghs9pd>.
- [15] la Cour-Harbo, A., "Quantifying Risk of Ground Impact Fatalities for Small Unmanned Aircraft," Vol. 93, No. 1-2, 2019, pp. 367–384. <https://doi.org/10.1007/s10846-018-0853-1>, URL <http://link.springer.com/10.1007/s10846-018-0853-1>.
- [16] Feyzabadi, S., and carpin, s., *Risk-Aware Path Planning Using Hierarchical Constrained Markov Decision Processes*, Vol. 2014, 2014. <https://doi.org/10.1109/CoASE.2014.6899341>.
- [17] Primatesta, S., Spanò Cuomo, L., Guglieri, G., and Rizzo, A., "An Innovative Algorithm to Estimate Risk Optimum Path for Unmanned Aerial Vehicles in Urban Environments," Vol. 35, 2018, pp. 44–53. <https://doi.org/10/ghs9pc>.
- [18] Primatesta, S., Guglieri, G., and Rizzo, A., "A Risk-Aware Path Planning Strategy for UAVs in Urban Environments," Vol. 95, No. 2, 2019, pp. 629–643. <https://doi.org/10/ghs9n9>, URL <https://doi.org/10.1007/s10846-018-0924-3>.
- [19] Guglieri, G., Lombardi, A., and Ristorto, G., "Operation Oriented Path Planning Strategies for Rpas," 2015. URL <https://core.ac.uk/display/76529019>.

- [20] Sutton, P. C., Elvidge, C., and Obremski, T., “Building and Evaluating Models to Estimate Ambient Population Density,” Vol. 69, No. 5, 2003, pp. 545–553. <https://doi.org/10.14358/PERS.69.5.545>.
- [21] for International Earth Science Information Network CIESIN Columbia University, C., *Gridded Population of the World, Version 4 (GPWv4): Population Density, Revision 11*, NASA Socioeconomic Data and Applications Center (SEDAC), ??? URL <https://doi.org/10.7927/H49C6VHW>.
- [22] Martin, D., Cockings, S., and Leung, S., “Developing a Flexible Framework for Spatiotemporal Population Modeling,” Vol. 105, No. 4, 2015, pp. 754–772. <https://doi.org/10.1080/00045608.2015.1022089>, URL <https://doi.org/10.1080/00045608.2015.1022089>.
- [23] OpenStreetMap contributors, “Planet Dump Retrieved from <https://planet.osm.org>,” 2017. URL <https://www.openstreetmap.org>.
- [24] “Average Commute and Percentage Travelling by Car for the UK and Constituent Countries - Office for National Statistics,” 2020. URL <https://www.ons.gov.uk/employmentandlabourmarket/peopleinwork/employmentandemployeetypes/adhocs/008986averagecommuteandpercentagetravellingbycarfortheukandconstituentcountries>.
- [25] “Nomis - Official Labour Market Statistics - Nomis - Official Labour Market Statistics,” 2020. URL <https://www.nomisweb.co.uk/query/construct/summary.asp?mode=construct&version=0&dataset=143>.
- [26] “Census Boundary Data,” 2011. URL <https://census.ukdataservice.ac.uk/get-data/boundary-data.aspx>.
- [27] Holt, J. B., Lo, C. P., and Hodler, T. W., “Dasymetric Estimation of Population Density and Areal Interpolation of Census Data,” Vol. 31, No. 2, 2004, pp. 103–121. <https://doi.org/10/b36jv3>, URL <https://doi.org/10.1559/1523040041649407>.
- [28] “Road Traffic Statistics (TRA),” 2020. URL <https://www.gov.uk/government/statistical-data-sets/road-traffic-statistics-tra>.
- [29] “Road Traffic Statistics - Download Data,” 2020. URL <https://roadtraffic.dft.gov.uk/downloads>.
- [30] “Vehicle Mileage and Occupancy,” 2020. URL <https://www.gov.uk/government/statistical-data-sets/nts09-vehicle-mileage-and-occupancy>.
- [31] Smith, P., “Expected Casualty Calculations For Commercial Space Launch and Reentry Missions,” 2000.
- [32] Dalamagkidis, K., Valavanis, K., and Piegl, L., “On Unmanned Aircraft Systems Issues, Challenges and Operational Restrictions Preventing Integration into the National Airspace System,” Vol. 44, No. 7-8, 2008, pp. 503–519. <https://doi.org/10.1016/j.paerosci.2008.08.001>, URL <https://linkinghub.elsevier.com/retrieve/pii/S0376042108000729>.
- [33] Westat Inc Rockville Md, “Range Safety Criteria for Unmanned Air Vehicles Rationale and Methodology Supplement:,” 2001. <https://doi.org/10.21236/ADA385238>, URL <http://www.dtic.mil/docs/citations/ADA385238>.
- [34] Van Rossum, G., and Drake, F. L., *Python 3 Reference Manual*, CreateSpace, 2009.
- [35] Reback, J., McKinney, W., jbrockmendel, den Bossche, J. V., Augspurger, T., Cloud, P., gyoung, Hawkins, S., Sinhrks, Roeschke, M., Klein, A., Petersen, T., Tratner, J., She, C., Ayd, W., Naveh, S., Garcia, M., Schendel, J., Hayden, A., Saxton, D., Jancauskas, V., patrick, McMaster, A., Battiston, P., Seabold, S., Dong, K., family=b1, u., prefix=chris, family=veterinari, u., prefix=h, Hoyer, S., and Gorelli, M., “Pandas-Dev/Pandas: Pandas 1.2.0,” 2020. <https://doi.org/10.5281/zenodo.4394318>, URL <https://zenodo.org/record/4394318>.
- [36] Jordahl, K., den Bossche, J. V., Fleischmann, M., Wasserman, J., McBride, J., Gerard, J., Tratner, J., Perry, M., Badaracco, A. G., Farmer, C., Hjelle, G. A., Snow, A. D., Cochran, M., Gillies, S., Culbertson, L., Bartos, M., Eubank, N., maxalbert, Bilogur, A., Rey, S., Ren, C., Arribas-Bel, D., Wasser, L., Wolf, L. J., Journois, M., Wilson, J., Greenhall, A., Holdgraf, C., Filipe, and Leblanc, F., “Geopandas/Geopandas: V0.8.1,” 2020. <https://doi.org/10.5281/zenodo.3946761>, URL <https://zenodo.org/record/3946761>.
- [37] JARUS WG-6 SORA Annex F Quantitative Methods subgroup, “CasEx: Casual Expectation Toolbox in Python,” 2021. URL casex.readthedocs.io.
- [38] Rudiger, P., Bednar, J. A., Stevens, J.-L., B, C., Little, B., Andrew, Signell, J., marqh, Bosley, C., Hattersley, R., Brener, G., ea42gh, kbowen, Hilboll, A., Lustig, I., Hand, N., Signell, R., Bampton, J., scaine1, and zassa, “Holoviz/Geoviews: Version 1.8.0,” 2020. <https://doi.org/10.5281/zenodo.4046982>, URL <https://zenodo.org/record/4046982>.
- [39] Rudiger, P., Stevens, J.-L., Bednar, J. A., Nijholt, B., Mease, J., Andrew, B, C., Randelhoff, A., Tenner, V., maxalbert, Kaiser, M., ea42gh, Samuels, J., stonebig, LB, F., Pevey, K., Tolmie, A., Stephan, D., Bois, J., Lowe, S., Bampton, J., henriqueribeiro, ruoyu0088, Lustig, I., Klein, A., de Ven, B. V., Signell, J., Talirz, L., Barth, L., and Lique, M., “Holoviz/Holoviews: Version 1.14.0,” 2020. <https://doi.org/10.5281/zenodo.4304750>, URL <https://zenodo.org/record/4304750>.

- [40] “[ARCHIVED CONTENT] Output Area (OA) - ONS,” , 2011. URL <https://webarchive.nationalarchives.gov.uk/20160107193025/http://www.ons.gov.uk/ons/guide-method/geography/beginner-s-guide/census/output-area--oas-/index.html>.
- [41] Deville, P., Linard, C., Martin, S., Gilbert, M., Stevens, F. R., Gaughan, A. E., Blondel, V. D., and Tatem, A. J., “Dynamic Population Mapping Using Mobile Phone Data,” Vol. 111, No. 45, 2014, pp. 15888–15893. <https://doi.org/10/wqh>, URL <https://www.pnas.org/content/111/45/15888>.
- [42] “Skyports - Infrastructure for Advanced Air Mobility,” , 2021. URL <https://skyports.net/>.
- [43] Grote, M., Cherrett, T., Oakey, A., Royall, P. G., Whalley, S., and Dickinson, J., “How Do Dangerous Goods Regulations Apply to Uncrewed Aerial Vehicles Transporting Medical Cargos?” Vol. 5, No. 2, 2021, p. 38. <https://doi.org/10/gj43xg>, URL <https://www.mdpi.com/2504-446X/5/2/38>.
- [44] Fukuda, K., “Interpolation and Forecasting of Population Census Data,” Vol. 27, No. 1, 2010, pp. 1–13. <https://doi.org/10/fb849d>.
- [45] Pilko, A., and Tait, Z., “Aliaksei135/Seedpod_ground_risk: V0.13.0,” , 2021. <https://doi.org/10.5281/zenodo.4776529>, URL <https://zenodo.org/record/4776529>.
- [46] “From Twitter to Traffic Predictor: Next-Day Morning Traffic Prediction Using Social Media Data,” 2020. <https://doi.org/10.1016/j.trc.2020.102938>, URL https://www.sciencedirect.com/science/article/pii/S0968090X20308354?dcid=rss_sd_all&utm_source=researcher_app&utm_medium=referral&utm_campaign=RESR_MRKT_Researcher_inbound.
- [47] Boeing, “Statistical Summary of Commercial Jet Airplane Accidents,” , 2020. URL http://www.boeing.com/resources/boeingdotcom/company/about_bca/pdf/statsum.pdf.